LiSBOA: LiDAR Statistical Barnes Objective Analysis for optimal design of LiDAR scans and retrieval of wind statistics. Part I: Theoretical framework

Stefano Letizia, Lu Zhan, and Giacomo Valerio Iungo

Wind Fluids and Experiments (WindFluX) Laboratory, Mechanical Engineering Department, The University of Texas at Dallas, 800 W Campbell Rd, 75080 Richardson, TX, USA

Correspondence: Giacomo Valerio Iungo, email: valerio.iungo@utdallas.edu

Abstract. A LiDAR Statistical Barnes Objective Analysis (LiSBOA) for optimal design of LiDAR scans and retrieval of the velocity statistical moments is proposed. The LiSBOA represents an adaptation of the classical Barnes scheme for the statistical analysis of unstructured experimental data in N-dimensional spaces and it is a suitable technique for the evaluation over a structured Cartesian grid of the statistics of scalar fields sampled through scanning LiDARs. The LiSBOA is validated
5 and characterized via a Monte Carlo approach applied to a synthetic velocity field. This revisited theoretical framework for the Barnes objective analysis enables the formulation of guidelines for optimal design of LiDAR experiments and efficient application of the LiSBOA for the post-processing of LiDAR measurements. The optimal design of LiDAR scans is formulated as a two cost-function optimization problem including the minimization of the percentage of the measurement volume not sampled with adequate spatial resolution and the minimization of the error on the mean of the velocity field. The optimal
10 design of the LiDAR scans also guides the selection of the smoothing parameter and the total number of iterations to use for the Barnes scheme.

1 Introduction

Reliable measurements of the wind-velocity vector field are essential to understand the complex nature of atmospheric turbulence and provide valuable datasets for the validation of theoretical and numerical models. However, field measurements of wind speed are typically characterized by large uncertainties due to the generally unknown and uncontrollable boundary
15 conditions (Braham, 1979), the broad range of time and length-scales (Cushman-Roisin and Beckers, 1990a), and the complexity of the physics involved (Stull, 1988). Furthermore, the large measurement volume, which typically extends throughout the height of the atmospheric boundary layer, imposes to the experimentalists the selection of the sampling parameters as a trade-off between spatial and temporal resolutions.

20 Wind speed has been traditionally measured through local sensors, such as mechanical, sonic, and hot-wire anemometers (Liu et al., 2019; Kunkel and Marusic, 2006). Besides their simplicity, mechanical anemometers are affected by errors due to the flow distortion of the supporting structures and harsh weather conditions (e.g. ice) (Mortensen, 1994). Furthermore, their relatively slow response results in a limited range of the measurable time-length scales, which makes them unsuitable, for

instance, to measure the turbulent flow around urban areas (Pardyjak and Stoll, 2017). Sonic anemometers can measure the
three velocity component with frequencies up to 100 Hz (Cuerva and Sanz-Andrés, 2000) in a probing volume of the order
of 0.01 m, yet measurements might be still affected by the wakes generated by the supporting structures, such as met-towers
and struts and they are sensitive to temperature variations (Mortensen, 1994). Hot-wire anemometers, although they provide a
full characterization of the energy spectrum, require a complicated calibration (Kunkel and Marusic, 2006) and are extremely
fragile (Wheeler, 2004). Furthermore, traditional single-point sensors are unable to provide an adequate characterization of the
spatial gradients of the wind velocity vector, which is particularly significant in the vertical direction (Cushman-Roisin and
Beckers, 1990b). To overcome this issue, several anemometers arranged in arrays and supported by meteorological masts have
been deployed in several field campaigns (Haugen et al., 1971; Bradley, 1983; Taylor and Teunissen, 1987; Emeis et al., 1995;
Pashow et al., 2001; Berg et al., 2011; Kunkel and Marusic, 2006).

In the last few decades, remote sensing instruments have been increasingly utilized to probe the atmospheric boundary
layer (Debnath et al., 2017b, a) and nowadays they represent a more cost-effective and flexible alternative to meteorological
towers (Newsom et al., 2017). In particular, in the realm of remote sensing anemometry, Doppler wind light detection and
ranging (LiDAR) systems underwent a rapid development due to the significant advancement in eye-safe laser technology
Emeis (2010). Wind LiDARs have been heavily employed in wind energy (Bingöl et al., 2010; Aitken and Lundquist, 2014;
Trujillo et al., 2011; Iungo et al., 2013; Machefaux et al., 2016; Garcia et al., 2017; El-Asha et al., 2017; Bromm et al., 2018;
Zhan et al., 2019, 2020), airport monitoring (Köpp et al., 2005; Tang et al., 2011; Holzäpfel et al., 2016; Thobois et al., 2019),
micro-meteorology (Gal-Chen et al., 1992; Banakh et al., 1999; Banta et al., 2006; Mann et al., 2010; Muñoz-Esparza et al.,
2012; Rajewski et al., 2013; Schween et al., 2014), urban wind research (Davies et al., 2007; Newsom et al., 2008; Xia et al.,
2008; Kongara et al., 2012; Huang et al., 2017; Halios and Barlow, 2018) and studies of terrain-induced effects (Bingöl, 2009;
Krishnamurthy et al., 2013; Kim et al., 2016; Pauscher et al., 2016; Risan et al., 2018; Fernando et al., 2019; Bell et al., 2020).

Besides the mentioned capabilities, LiDARs present some important limitations, such as reduced range in adverse weather
conditions (precipitations, heavy rain or low aerosol concentration) (Liu et al., 2019) and a limited spatio-temporal resolution
of this instrument, namely about 20 meters in the radial direction and about 10 Hz in sampling frequency. These technical
specifications, associated with the non-stationary wind conditions typically encountered for field experiments, pose major
challenges to apply wind LiDARs for the statistical analysis of turbulent atmospheric flows.

In the realm of wind energy, early LiDAR measurements were limited to the qualitative analysis of snapshots of the line-of-
sight (LOS) velocity, i.e. the velocity component parallel to the laser beam (Käsler et al., 2010; Clive et al., 2011). Fitting of
the wake velocity deficit was also successfully exploited to extract quantitative information about wake evolution from LiDAR
measurements (Aitken and Lundquist, 2014; Wang and Barthelmie, 2015; Kumer et al., 2015; Trujillo et al., 2016; Bodini
et al., 2017). To characterize velocity fields with higher statistical significance, the time averages of several LiDAR scans
were calculated for time periods with reasonably steady inflow conditions (Iungo and Porté-Agel, 2014; Machefaux et al.,
2016; Van Dooren et al., 2016). In the case of data collected under different wind and atmospheric conditions, clustering and
bin-averaging of LiDAR data were carried out (Machefaux et al., 2016; Garcia et al., 2017; Bromm et al., 2018; Zhan et al.,
2019, 2020). Finally, more advanced techniques for first-order statistical analysis, such as variational methods (Xia et al., 2008;

Newsom and Banta, 2004), optimal interpolation (Xu and Gong, 2002; Kongara et al., 2012), least-squares methods (Newsom

60 et al., 2008), Navier-Stokes solvers (Astrup et al., 2017; Sekar et al., 2018) were applied for the reconstruction of the velocity
vector field from dual-Doppler measurements.

Besides the mean field, the calculation of higher-order statistics from LiDAR data to investigate atmospheric turbulence is
still an open problem. In this regard, Eberhard et al. (1989) re-adapted the post-processing of the velocity azimuth display
(VAD) scans (Lhermitte, 1969; Wilson, 1970; Kropfli, 1986) to estimate all the components of the Reynolds stress tensor by

65 assuming horizontal homogeneity of the flow within the scanning volume, which can be a limiting constraint for measurements
in complex terrains (Bingöl, 2009; Frisch, 1991). Range height indicator (RHI) scans were used to detect second-order statistics
(Bonin et al., 2017), spectra, skewness, dissipation rate of the velocity field, and even heat flux (Gal-Chen et al., 1992).

A typical scanning strategy to obtain high-frequency LiDAR data consists in performing scans with fixed elevation and
azimuthal angles of the laser beam while maximizing the sampling frequency (Mayor et al., 1997; O'Connor et al., 2010;

70 Vakkari et al., 2015; Frehlich and Cornman, 2002; Debnath et al., 2017b; Choukulkar et al., 2017; Lundquist et al., 2017).
Recently, in the context of wind radar technology, but readily applicable to LiDARs as well, a promising method for the
estimation of the instantaneous turbulence intensity based on the Taylor hypothesis of frozen turbulence was proposed by
Duncan et al. (2019). More advanced techniques exploit additional information of turbulence carried by the spectrum of the
back-scattered LiDAR signal (Smalikho, 1995). However, this approach requires the availability of LiDAR raw data, which is

75 not generally granted for commercial LiDARs. For a review on turbulence statistical analyses through LiDAR measurements,
the reader can refer to Sathe and Mann (2013).

For remote sensing instruments, data are typically collected based on a spherical coordinate system, then interpolated over
a Cartesian reference frame oriented with the x-axis in the mean wind-direction. This interpolation can be a source of error
(Fuertes Carbajo and Porté-Agel, 2018), especially if a linear interpolation method is used (Garcia et al., 2017; Carbajo Fuertes

80 et al., 2018; Beck and Kühn, 2017; Astrup et al., 2017). Delaunay triangulation has also been widely adopted for coordinate
transformation (Clive et al., 2011; Trujillo et al., 2011; Iungo and Porté-Agel, 2014; Trujillo et al., 2016; Machefaux et al.,
2016), yet with accuracy not quantified in case of non-uniformly distributed data. It is reasonable to weight the influence of
the experimental points on their statistics by the distance from the respective grid centroid, such as using uniform (Newsom
et al., 2008), hyperbolic (Van Dooren et al., 2016) or Gaussian weights (Newsom et al., 2014; Wang and Barthelmie, 2015;

85 Zhan et al., 2019). The use of distance-based Gaussian weights for the interpolation of scattered data over a Cartesian grid is at
the base of the Barnes objective analysis (or Barnes scheme) (Barnes, 1964), which has been extensively used in meteorology.
It represents an iterative statistical ensemble procedure to reconstruct a scalar field arbitrarily sampled in space and low-pass
filtered with a cut-off wavelength that is a function of the parameters of the scheme.

The scope of this work is to define a methodology to post-process scattered data of a turbulent velocity field measured

90 through a scanning Doppler wind LiDAR to calculate mean, standard deviation and even higher-order statistical moments on a
Cartesian grid. The proposed methodology, referred to as LiDAR Statistical Barnes Objective Analysis (LiSBOA), represents
an adaptation of the classic Barnes scheme to N-dimensional domains enabling applications for non-isotropic scalar fields
through a coordinate transformation. A major point of novelty of the LiSBOA is the estimation of wind-velocity variance

(and eventually higher-order statistics) from the residual field of the mean, which also provides adequate filtering of dispersive
stresses due to data variability not connected with the turbulent motion. A criterion for rejection of statistical data affected
by aliasing due to the undersampling of the spatial wavelengths under investigation is formulated. The LiSBOA is assessed
against a synthetic scalar field to validate its theoretical response and the formulated error metric. Finally, detailed guidelines
for the optimal design of a LiDAR experiment and effective reconstruction of the wind statistics are provided.

The remainder of the manuscript is organized as follows: in Sect. 2 the extension of the Barnes scheme theory to N-dimensional domains and higher-order statistical moments is presented. In Sect. 3, the theoretical response function of the
LiSBOA is validated against a synthetic case, while guidelines for proper use of the proposed algorithm are provided in Sect.
4. Finally, concluding remarks are provided in Sect. 5.

2   The Barnes Objective Analysis: fundamentals and extension to statistical N-dimensional analysis

The Barnes scheme was originally conceived as an iterative algorithm aiming to interpolate a set of sparse data over a Cartesian
grid (Barnes, 1964) and it was inspired by the successive correction scheme by Cressman (1959). The first iteration of the
algorithm calculates a weighted-space-averaged field, g^0, over a Cartesian grid from the sampled scalar field, f. The mean field
is iteratively modified by adding contributions to recover features characterized by shorter wavelengths, which are inevitably
damped by the initial averaging process. In this work, we adopt the most classical form of the Barnes scheme as follows:

$$
\begin{cases}
g_i^0 = \sum_j w_{ij} f_j \\
g_i^m = \sum_j w_{ij} (f_j - \phi(g^{m-1})_j) + g_i^{m-1} \quad \forall \quad m \in \mathbb{N}^+,
\end{cases}
\tag{1}
$$

where g_i^m is the average field at the i-th grid node with coordinates $\boldsymbol{r_i}$ for the m-th iteration, f_j is the scalar field sampled at
the location $\boldsymbol{r_j}$ and ϕ represents the linear interpolation operator from the Cartesian grid to the sample location. The weights
for the sample acquired at the location $\boldsymbol{r_j}$ and for the calculation of the statistics of f at the grid node with coordinates $\boldsymbol{r_i}$, w_{ij},
are defined as:

$$
w_{ij} = \frac{e^{-\frac{|\boldsymbol{r_i} - \boldsymbol{r_j}|^2}{2\sigma^2}}}{\sum_j e^{-\frac{|\boldsymbol{r_i} - \boldsymbol{r_j}|^2}{2\sigma^2}}},
\tag{2}
$$

where σ is referred to as smoothing parameter and $|.|$ indicates Euclidean norm. For practical reasons, the summations over j
are performed over the neighboring points included in a ball with a finite radius $R_{\max}$ (also called the radius of influence) and
centered at the i-th grid point. In this work, following Barnes (1964), we selected $R_{\max} = 3\sigma$, which encompasses 99.7% and
97% of the volume of the weighting function in 2D and 3D, respectively.

In literature, there is a lack of consensus for the selection of the total number of iterations (Barnes, 1964; Achtemeier,
1989; Smith and Leslie, 1984; Seaman, 1989) and the smoothing parameter (Barnes, 1994a; Caracena, 1987; Pauley and Wu,
1990). A reduction of the smoothing parameter, σ, as a function of the iteration, m, was originally proposed by Barnes (1973);
however, this approach resulted to be detrimental in terms of noise suppression (Barnes, 1994c).

In the frequency domain, the Barnes objective analysis is tractable as a low-pass filter applied to a scalar field, f, with a response as a function of the spatial wavelength depending on the smoothing parameter, σ, and the number of iterations, m.

125 This feature has been exploited in meteorology to separate small-scale from mesoscale motions (Doswell, 1977; Maddox, 1980; Gomis and Alonso, 1990). The spectral behavior of the Barnes scheme has been traditionally characterized by calculating the so-called continuous response at the m-th iteration, $D^m(\boldsymbol{k})$, with $\boldsymbol{k}$ being the wavenumber vector. $D^m(\boldsymbol{k})$ is defined as the ratio between the amplitude of the Fourier mode $e^{\mathrm{i}\boldsymbol{k}\cdot\boldsymbol{x}}$ (with $\mathrm{i} = \sqrt{-1}$) for the reconstructed field, g^m, to its amplitude for in input field, f, in the limit of a continuous distribution of samples and infinite domain. The analytical expression for the continuous

130 response was provided by Barnes (1964) and Pauley and Wu (1990) for 1D and 2D domains, respectively, while in the context of the LiSBOA it is extended to N dimensions to enhance its applicability. Furthermore, besides the spatial variability of f, the temporal coordinate, t, is introduced to determine the response of the statistical moments of f. Although the present discussion hinges on the choice of time as a non-spatial variable, the same approach can be applied to other non-spatial variables, such as Obukhov length to characterize atmospheric stability, operative conditions of a wind turbine, wind direction, assuming that

135 statistical homogeneity holds along that coordinate.

We consider a continuous scalar field, $f(\boldsymbol{x},t)$, which is defined over an N-dimensional domain, $\boldsymbol{x}$. It is further assumed that the field f is ergodic in time. By adopting the approach proposed by Pauley and Wu (1990) and by taking advantage of the isotropy of the Gaussian weights (Eq. (2)), we can define the LiSBOA operator at the 0-th iteration as:

$$g^0(\boldsymbol{x}) = \frac{1}{(\sqrt{2\pi}\sigma)^N} \int\limits_{\mathbb{R}^N} \left[\frac{1}{t_2 - t_1} \int\limits_{t_1}^{t_2} f(\boldsymbol{\xi},t)dt \right] e^{-\frac{|\boldsymbol{x}-\boldsymbol{\xi}|^2}{2\sigma^2}} d\boldsymbol{\xi}, \tag{3}$$

140 where t_1 and t_2 are initial and final time. The term within the square brackets represents the mean of f over the considered sampling interval $[t_1,\ t_2]$, which is indicated as $\overline{f}$. Moreover, to reconstruct a generic q-th central statistical moment of the scalar field, f, it is sufficient to apply the LiSBOA operator of Eq. (3) to the fluctuations over $\overline{f}$ to the q-th power:

$$\mu_f^q(\boldsymbol{x}) = \frac{1}{(\sqrt{2\pi}\sigma)^N} \int\limits_{\mathbb{R}^N} \left\{ \frac{1}{t_2 - t_1} \int\limits_{t_1}^{t_2} \left[f(\boldsymbol{\xi},t) - \overline{f}(\boldsymbol{\xi},t) \right]^q dt \right\} e^{-\frac{|\boldsymbol{x}-\boldsymbol{\xi}|^2}{2\sigma^2}} d\boldsymbol{\xi}. \tag{4}$$

For practical applications, the mean field $\overline{f}$ is generally not known, but it can be approximated by the LiSBOA output, g^m,

145 interpolated at the sample location through the operator ϕ. By comparing Eq. (4) with Eq. (3), it is understandable that the response function of any central moment with order higher than one is equal to that of the 0-th iteration response of the mean, g^0. Indeed, Eq. (3) can be interpreted as the 0-th iteration of the LiSBOA spatial operator (viz. Eq. (3)) applied to the fluctuation field to the q-th power.

By leveraging the convolution theorem, it is possible to calculate the response function of the mean of the 0-th iteration of

150 the LiSBOA in the frequency domain (see Appendix A for more details). This result, combined with the recursive formula of Barnes (1964) for the response at the generic iteration m, provides the spectral response of the LiSBOA for the mean:

$$D^m = \begin{cases} D^0(\boldsymbol{k}) = e^{-\frac{\sigma^2}{2}|\boldsymbol{k}|^2} = e^{-\frac{\sigma^2\pi^2}{2}\left[\sum_{p=1}^{N} \frac{1}{\Delta n_p^2} \right]} & \text{for } m = 0 \\ D^0 \sum_{p=0}^{m} (1 - D^0)^p & \text{for } m \in \mathbb{N}^+, \end{cases} \tag{5}$$

where $\boldsymbol{\Delta n}$ is the half-wavelength vector associated with $\boldsymbol{k}$. Equation 5 states that, for a given wavenumber (i.e. half-wavelength), the respective amplitude of the interpolated scalar field, g^m, is equal to that of the original scalar field, damped with a function

155 of the smoothing parameter, σ, and the number of iterations, m. This implies that the parameters σ and m should be selected properly to avoid significant damping for wavelengths of interest or dominating the spatial variability of the scalar field under investigation.

For real applications, the actual LiSBOA response function can depart from the above-mentioned theoretical response (Eq. (5)) for the following reasons:

160 - the convolution integral in Eq. (3) is calculated over a ball of finite radius $R_{\max}$;

- f is sampled over a discrete domain and, thus, introducing related limitations, such as the risk of aliasing (Pauley and Wu, 1990);

- the distribution of the sampling points is usually irregular and non-uniform leading to larger errors where a lower sample density is present (Smith et al., 1986; Smith and Leslie, 1984; Buzzi et al., 1991; Barnes, 1994a) or in proximity to the

165 domain boundaries (Achtemeier, 1986);

- an error is introduced by the back-interpolation function, ϕ, from the Cartesian grid, $\boldsymbol{r_i}$, to the location of the samples, $\boldsymbol{r_j}$ (Eq. (1)) (Pauley and Wu, 1990).

Before proceeding with further analysis, it is necessary to address the applicability of the LiSBOA to anisotropic and multi-chromatic scalar fields. Generally, the application of the LiSBOA with an isotropic weighting function is not recommended in

170 case of severe anisotropy of the field and/or the data distribution. At the early stages of objective analysis techniques, the use of an anisotropic weighting function was proved to be beneficial to increase accuracy while highlighting patterns elongated along a specific direction, based on empirical (Endlich and Mancuso, 1968) and theoretical arguments (Sasaki, 1971). Furthermore, the adoption of a directional smoothing parameter, σ_p, where p is a generic direction, allows maximizing the utilization of the data retrieved through inherently anisotropic measurements, such as the line-of-sight fields detected by remote sensing

175 instruments (Askelson et al., 2000; Trapp and Doswell, 2000). With this in mind, we propose a linear scaling of the physical coordinates before the application of the LiSBOA to recover a pseudo-isotropic velocity field. The scaling reads as:

$$\tilde{x}_p = \frac{x_p - x_p^*}{\Delta n_{0,p}}, \tag{6}$$

where $\boldsymbol{x}^*$ is the origin of the scaled reference frame and $\Delta n_{0,p}$ is the scaling factor for the p-th direction. Hereinafter, $\tilde{\ }$ refers to the scaled frame of reference. From a physical standpoint, the scaling is equivalent to the adoption of an anisotropic

180 weighting function, while the re-scaling approach is preferred to ensure generality to the mathematical formulation outlined in this section.

The scaling factor, $\boldsymbol{\Delta n_0}$, is an important parameter in the present framework and is referred to as fundamental half-wavelength, while the associated Fourier mode is denoted as the fundamental mode. The selection of the fundamental half-wavelength should be guided by a priori knowledge of the dominant length-scales of the flow in various directions. Modes

exhibiting degrees of anisotropy different than that of the selected fundamental mode, will not be isotropic in the scaled mapping, which leads two consequences: first, their response will not be optimal, in the sense that the shortest directional wavelength can produce excessive damping of the specific mode (Askelson et al., 2000); second, the shape preservation of such non-spherical features in the field reconstructed through the LiSBOA is not ensured (Trapp and Doswell, 2000).

Regarding the reconstruction of the flow statistics through the LiSBOA, two categories of error can be identified. The first is the statistical error due to the finite number of samples of the scalar field, f, available in time. This error is strictly connected with the local turbulence statistics, the sampling rate, and the duration of the experiment. The second error category is the spatial sampling error, which is due to the discrete sampling of f in the spatial domain $\boldsymbol{x}$. The Petersen-Middleton theorem (Petersen and Middleton, 1962) states that the reconstruction of a continuous and band-limited signal from its samples is possible if and only if the spacing of the sampling points is small enough to ensure non-overlapping of the spectrum of the signal with his replicas distributed over the so-called reciprocal lattice (or grid). The latter is defined as the Fourier transform of the specific sampling lattice. The 1D version of this theorem is the well-known Shannon-Nyquist theorem (Shannon, 1984). An application of this theorem to non-uniformly distributed samples, like those measured by remote sensing instruments, is unfeasible due to the lack of periodicity of the sampling points. To circumvent this issue, we adopted the approach suggested by Koch et al. (1983), who defined the random data spacing, Δd, as the equivalent distance that a certain number of samples enclosed in a certain region, N_{exp}, would have if they were uniformly distributed over a structured Cartesian grid. The generalized form of the random data spacing reads:

$$\Delta d(\boldsymbol{r_i}) = \frac{V^{\frac{1}{N}}}{N_{\text{exp}}(\boldsymbol{r_i})^{\frac{1}{N}} - 1}, \tag{7}$$

where V is the volume of the hyper-sphere with radius $R_{\max} = 3\sigma$ centered at the specific grid point and N_{exp} represents the number of not co-located sample locations included within the hyper-sphere. Then, the Petersen-Middleton theorem for the reconstruction of the generic Fourier mode of half-wavelength $\boldsymbol{\Delta n}$ can be translated as the following constraint:

$$\Delta d(\boldsymbol{r_i}) < \Delta n_p, \ p = 1, 2, ..., N. \tag{8}$$

Violation of the inequality (8) will lead to local aliasing, with the energy content of the under-sampled wavelengths being added to the low-frequency part of the spectrum.

3 LiSBOA assessment through Monte Carlo simulations

The spectral response of the LiSBOA is studied through the Monte Carlo method. The goal of the present section is twofold: validating the analytical response of mean and variance (Eq. (5)) and characterizing the sampling error of the LiSBOA as a function of the random data spacing. For these aims, a synthetic 3D scalar field is generated, while its temporal variability is reproduced locally by randomly sampling a normal probability density function. Specifically, the synthetic scalar field is:

$$f = \left[1 + \sin\left(\frac{\pi}{\Delta n}x\right)\sin\left(\frac{\pi}{\Delta n}y\right)\sin\left(\frac{\pi}{\Delta n}z\right)\right] + \left[1 + \sin\left(\frac{\pi}{\Delta n}x\right)\sin\left(\frac{\pi}{\Delta n}y\right)\sin\left(\frac{\pi}{\Delta n}z\right)\right]^{0.5} \aleph(0, 1), \tag{9}$$

215   where ℵ is a generator of random numbers with normal probability density function with mean value 0 and standard deviation
equal to 1. The constant 1 in the two terms on the RHS of Eq. (9) does not affect the LiSBOA response and is introduced to
obtain both mean and variance of f equal to the following function:

$$\overline{f} = 1 + \sin\left(\frac{\pi}{\Delta n}x\right)\sin\left(\frac{\pi}{\Delta n}y\right)\sin\left(\frac{\pi}{\Delta n}z\right). \tag{10}$$

It is noteworthy that $\overline{f} - 1$ is a monochromatic isotropic function.

220   An experimental sampling process is mimicked by evaluating the scalar field f through randomly and uniformly distributed
samples collected at the locations r_j. The latter are distributed within a cube spanning the range $\pm 10\sigma$ in the three Cartesian
directions. The total number of sampling points considered for each realization, N_s, is varied from 500 up to 20,000 to explore
the effects of the sample density on the error. The sampling process is repeated L times for each given distribution of N_s points
to capture the variability in the field introduced by the operator ℵ. The whole procedure can be considered as an idealized
225   LiDAR experiment where a scan including N_s sampling points is performed L times to probe an ergodic turbulent velocity
field.

Since the response is only a function of $\Delta n/\sigma$ and m (Eq. (5)), for the spectral characterization of the LiSBOA, the parameter
$\Delta n/\sigma$ is varied among the following values: [1, 2, 3, 4, 5]. An implementation of the LiSBOA algorithm for discrete samples
is then applied to reconstruct the mean g^m and variance v^m of the scalar field f over a Cartesian structured grid, r_i, with a
230   resolution of 0.25. Figure 1 depicts an example of the reconstruction of the mean scalar field, g^m, and its variance, v^m, from
the Monte Carlo synthetic dataset.

For the error quantification, the 95-th percentile of the absolute error calculated at each grid point r_i (AE_{95} hereinafter) is
adopted:

$$AE_{95}(\Delta n/\sigma, m, N_s, L) = \begin{cases} \text{percentile}_{95}\langle|(g^m - 1) - D^m(\overline{f} - 1)|\rangle_{r_i} & \text{for the mean} \\ \text{percentile}_{95}\langle|(v^m - 1) - D^0(\overline{f} - 1)|\rangle_{r_i} & \text{for the variance.} \end{cases} \tag{11}$$
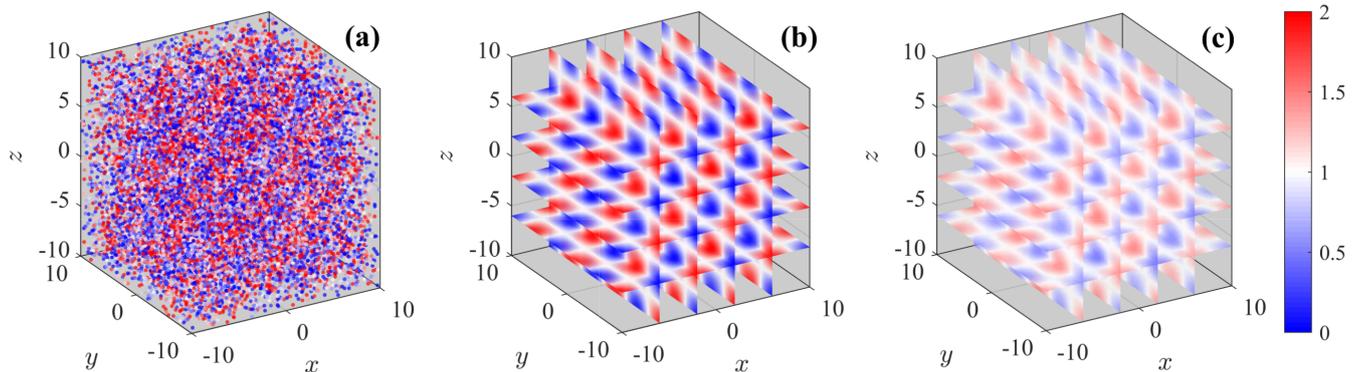
Figure 1. Visualization of the LiSBOA applied to a Monte Carlo simulation of the synthetic field in Eq. (9) for the case with $N_s = 20,000$,
$L = 200$, $\Delta n/\sigma = 4$ and $m = 5$: **(a)** samples; **(b)** 3D reconstructed mean field, g^m; **(c)** 3D reconstructed variance, v^m.

235 The AE_{95} quantifies the discrepancy between the outcome of the LiSBOA and the analytical input damped by the theoretical response evaluated over the Cartesian grid. As highlighted in Eq. (11), the expected value of AE_{95} is a function of the half-wavelength over the smoothing parameter, $\Delta n/\sigma$, the number of iterations, m, the number of samples, N_s, and the number of realizations, L. To investigate the link between AE_{95} and the above-mentioned parameters, the Pearson correlation coefficients are analyzed (Table 1). The number of samples N_s, which is inversely proportional to the data spacing Δd (Eq. 7), is the

240 variable exhibiting the strongest correlation with the error for both mean and variance. This indicates, as expected, that a larger number of samples for each measurement realization is always beneficial for the estimates of the statistics of the scalar field, f. Furthermore, the negative sign of correlations $\rho(AE_{95}, N_s)$ and $\rho(AE_{95}, \Delta n/\sigma)$, corroborate the hypothesis that the ratio $\Delta d/\Delta n$, i.e. the number of samples per half-wavelength, is the main driving factor for the sampling error (Koch et al., 1983; Barnes, 1994a; Caracena et al., 1984).

245 The small positive correlation $\rho(AE_{95}, m)$ detected for the mean is due to an amplification of the error occurring during the iterative process (Barnes, 1964). The issue will be discussed more in detail in Sect. 4. For the variance, $\rho(AE_{95}, m)$ is practically negligible, confirming that the response of the higher-order statistics is insensitive to the number of iterations, m. Finally, the negative correlations with L show that the statistical error is inversely proportional to the number of realizations collected. The dependence $\rho(AE_{95}, L)$ is mainly due to the statistical error connected with the temporal sampling and, thus, the

250 number of realizations, L, is progressively increased until convergence of the AE_{95} is achieved. Figure 2 displays the behavior of the error as a function of N_s and L. The values displayed represent the median for all the wavelength and iterations, being the AE_{95} just mildly dependent on these parameters. As Fig. 2 shows, increasing the number of realizations, L, beyond 100 has a negligible effect on the error, thus a final value of $L = 200$ is selected for the remainder of this analysis.

To verify the analytical response of mean and variance of the scalar field, f, a numerical estimator of the response is defined

255 as the median in space of the ratio between the field reconstructed via LiSBOA and the expected value of the synthetic input, as:

$$
\begin{cases}
D^m = \text{median}\langle \frac{g^m - 1}{\overline{f} - 1}\rangle_{\boldsymbol{r_i}} & \text{for the mean} \\
D^0 = \text{median}\langle \frac{v^m - 1}{\overline{f} - 1}\rangle_{\boldsymbol{r_i}} & \text{for the variance.}
\end{cases}
\tag{12}
$$

In the calculation of the numerical response through Eq. (12), the influence of the edges is removed by rejecting points closer than $R_{\max}$ to the boundaries of the numerical domain. Furthermore, the zero-crossings of the synthetic sine function ($|\overline{f} - 1| <$

Table 1. Pearson correlation coefficient between the AE_{95} of mean and variance and the parameters $\Delta n/\sigma$, m, N_s, L. The values between parenthesis represent the 95% confidence bounds.

	$\Delta n/\sigma$	m	N_s	L
AE_{95} of mean	-0.259 (-0.303, -0.210)	0.257 (0.211, 0.301)	-0.709 (-0.732, -0.684)	-0.171 (-0.217, -0.124)
AE_{95} of variance	-0.069 (-0.117, -0.021)	-0.03 (-0.078, 0.019)	-0.694 (-0.718, -0.668)	-0.206 (-0.251, -0.159)
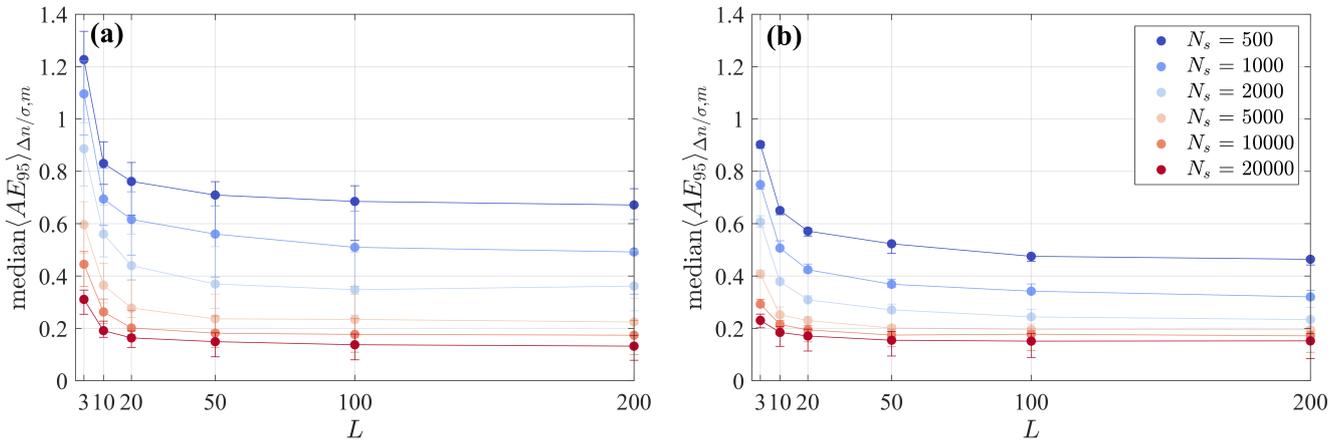
Figure 2. Median of the AE_{95} for all the tested half-wavelengths, $\Delta n/\sigma$, and the number of iterations, m: **(a)** AE_{95} of the mean field, g^m; **(b)** AE_{95} of the variance field, v^m. The error bars span the interquartile range.
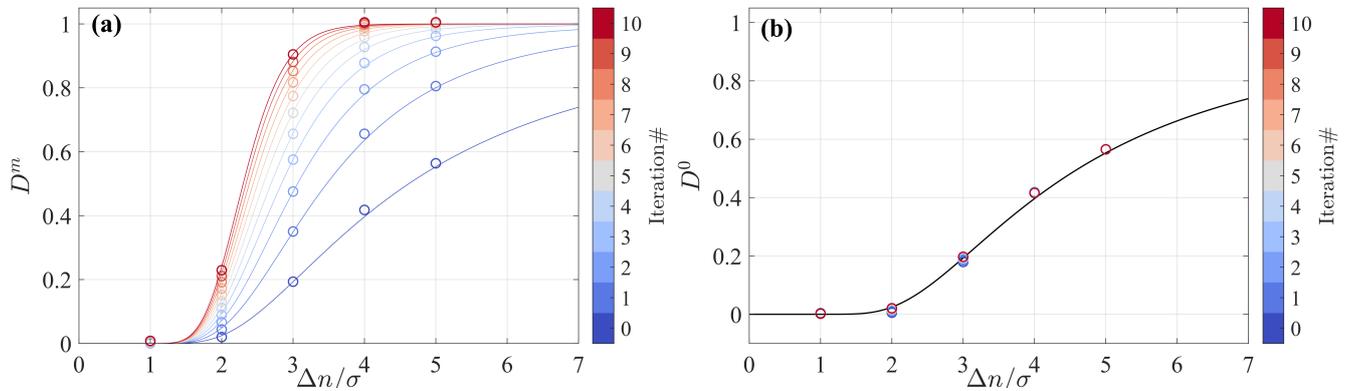
Figure 3. Validation of the 3D theoretical response of the LiSBOA for the case $N_s = 20000$ - $L = 200$: **(a)** mean; **(b)** variance. The circles are the numerical output of the Monte Carlo simulation (Eq. (12)), while the continuous lines represent Eq. (5).

260   0.1) are excluded to avoid singularities. A comparison between the actual and the theoretical response (Eq. (5)) for several wavelengths of the input function is reported in Fig. 3 for the case with the highest number of samples $N_s = 20,000$. An excellent agreement is observed between the theoretical prediction and the Monte Carlo outcome, which indicates that in the limit of negligible statistical error (large L) and adequate sampling (large N_s and near-uniformly distributed samples) the response approaches the predictions obtained from the developed theoretical framework.

265   The trend of the response of the mean (Fig. 3a suggests that, for a given wavelength, the same response can be achieved for an infinite number of combinations $\sigma - m$ and, specifically, a larger σ requires a larger number of iterations, m, to achieve a certain response D^m. It is noteworthy that for a smaller number of iterations, m, the slope of the response function is lower. This feature can be beneficial for practical applications for which the LiSBOA response will have small changes for small variations

of Δn. However, a lower slope of the response function can be disadvantageous for short-wavelength noise suppression. Figure 3b confirms that the response of the variance, and similarly for higher-order statistics, is not a function of the total number of iterations, m, and is equal to the response of the mean for the 0-th iteration, D^0.

Finally, the link between error and the random data spacing, Δd, is investigated. In Fig. 4, the discrepancy with respect to theory quantified by the AE_{95} is plotted versus the random data spacing normalized by the half-wavelength for a fixed total number of iterations $m = 5$. The values displayed on the x-axis represent the median over all grid points, $\mathbf{r_i}$. This analysis reveals a strong correlation between the normalized random data spacing and the error. This analysis corroborates that, in the limit of negligible statistical error (viz. a high number of realizations, L), uncertainty is mainly driven by the local data density normalized by the wavelength, which is related to the Petersen-Middleton criterion. Indeed, the cases satisfying the Petersen-Middleton constraint (Eq. (8)) are those exhibiting an AE_{95} smaller than $\sim 40\%$ of the amplitude of the harmonic function $\overline{f}$ for both mean and variance. However, if a smaller error is needed, it will be necessary to reduce the maximum threshold value for $\Delta d / \Delta n$.

4 Guidelines for an efficient application of the LiSBOA to wind LiDAR data

An efficient application of the LiSBOA to LiDAR data relies on the appropriate selection of the parameters of the algorithm, namely the fundamental half-wavelengths, $\mathbf{\Delta n_0}$, the smoothing parameter, σ, the number of iterations, m, and the spatial discretization of the Cartesian grid, $\mathbf{dx}$. Furthermore, the data collection strategy must be designed to ensure adequate sampling of the spatial wavelengths of interest, so that the Petersen-Middleton constraint (Eq. (8)) is satisfied. In this section, we show that the underpinning theory of the LiSBOA, along with an estimate of the fundamental properties of the flow under investigation, can guide the optimal design of a LiDAR experiment and evaluation of the statistics for a turbulent ergodic flow. The whole
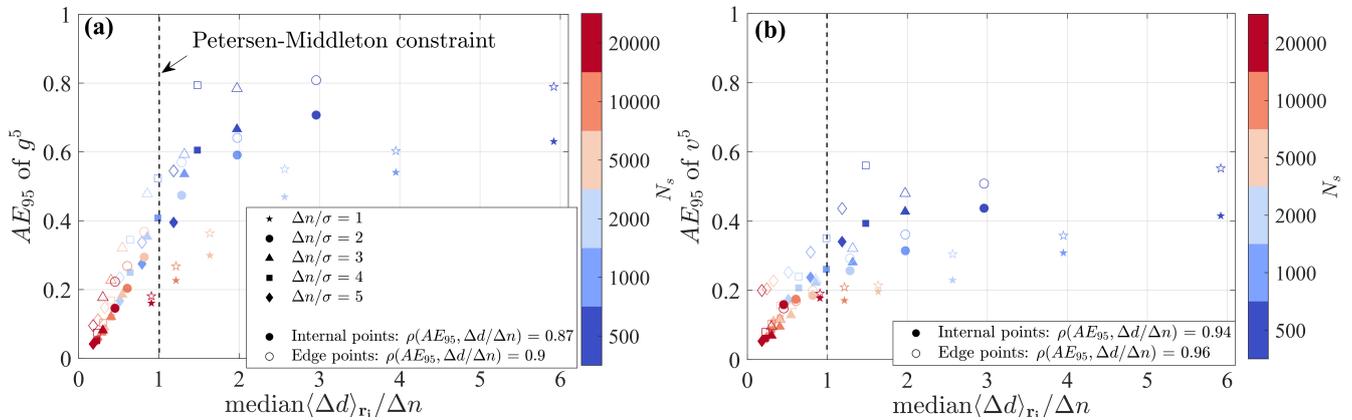
Figure 4. AE_{95} as a function of the random data spacing (Eq. (7)) for the case with $m = 5$, $N = 20000$ and $L = 200$: **(a)** error on the mean; **(b)** error on the variance. The full symbols refer to points not affected by the presence of the finite boundaries of the domain, while the empty symbols are taken within a distance of less than R_{max} from the boundaries.

procedure can be divided into three phases: characterization of the flow, design of the experiment, and reconstruction of the statistics from the collected dataset.

290   Firstly, it is crucial to estimate the integral quantities of the flow under investigation required for the application of the LiSBOA, such as extension of the spatial domain of interest, characteristic length-scales, integral time-scale, τ, characteristic temporal standard deviation of the velocity, $\sqrt{\overline{u'^2}}$, and expected total sampling time, T, which depends on the typical duration of stationary boundary conditions over the domain. These estimates can be based on previous studies available in literature, numerical simulations, or preliminary measurements.

295   Then, it is necessary to define the fundamental half-wavelengths, $\boldsymbol{\Delta n_0}$, which are required for the coordinate scaling (Eq. (6)). It is advisable to impose the fundamental half-wavelengths equal to (or even smaller than) the estimated characteristic length-scales of the smallest spatial features of interest in the flow. This ensures isotropy of the mode associated with the fundamental half-wavelength (and all the modes characterized by the same degree of anisotropy) and guides the selection of the main input parameters of the LiSBOA algorithm, i.e. smoothing parameter, σ, and number of iterations, m. Indeed, $\boldsymbol{\Delta n_0}$

300   can be considered as the cut-off half-wavelength of the spatial low-pass filter represented by the LiSBOA operator. To this aim, it is necessary to select σ and m to obtain a response of the mean associated with the fundamental mode, $D^m(\boldsymbol{\Delta \tilde{n}_0})$, as close as possible to 1. After the coordinate scaling (Eq. (6)), the response of the fundamental mode is universal and it is reported in Fig. 5. For instance, if we select a response equal to 0.95, then all the points lying on the iso-contour defined by the equality $D^m(\boldsymbol{\Delta \tilde{n}_0}) = 0.95$ give, in theory, the same response for the mean of the scalar field f. This implies that an infinite number

305   of combinations $\sigma - m$ allow obtaining a response of the mean equal to the selected value. However, with increasing σ the response at the 0-th iteration, $D^0(\boldsymbol{\Delta \tilde{n}_0})$, reduces, which indicates a lower response for higher-order statistics. For the LiSBOA application, the following aspects should be also considered:
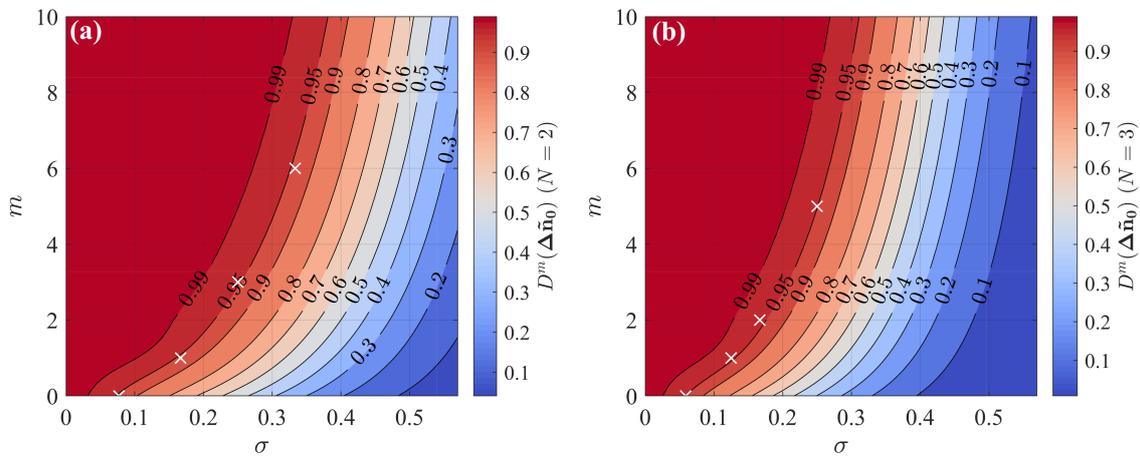
Figure 5. Response of the fundamental mode in the scaled coordinates as a function of the number of iterations and the smoothing parameter: **(a)** two-dimensional LiSBOA; **(b)** three-dimensional LiSBOA. The white crosses indicate the pairs $\sigma - m$ provided in Table 2.

    – the smaller σ, the smaller the radius of influence of the LiSBOA, $R_{\max}$, and, thus, the lower the number of samples averaged per grid node, $N_{\exp}$, and the greater the statistical uncertainty;

310   – an excessively large m can lead to overfitting of the experimental data and noise amplification (Barnes, 1964);

    – the higher m, the higher the slope of the response function (see Fig. 3), which improves the damping of high-frequency noise, but it produces a larger variation of the response of the mean with different spatial wavelengths;

    – the radius of influence $R_{\max}$ (and therefore σ) can affect the data spacing Δd in case of non-uniform data distribution.

Few handy combinations of smoothing parameter and total iterations for $D^m(\boldsymbol{\Delta}\tilde{\boldsymbol{n}}_0) = 0.95$ are provided in Table 2. As men-
315 tioned above, all these $\sigma - m$ pairs allow achieving roughly the same response for the mean, while the response for the higher-order statistics reduces with an increasing number of iterations, m.

As a final remark about the selection of $\boldsymbol{\Delta n_0}$, we should consider that, if the fundamental half-wavelength is too large compared to the dominant modes in the flow, small-scale spatial oscillations of f will be smoothed out during the calculation of the mean, with consequent underestimated gradients and incorrect estimates of the high-order statistics due to the dispersive
320 stresses (Arenas et al., 2019). On the other hand, the selection of an overly small $\boldsymbol{\Delta n_0}$, would require an excessively fine data spacing to satisfy the Petersen-Middleton constraint (Eq. (8)), which may lead to an overly long sampling time or even exceed the sampling capabilities of the LiDAR.

The optimal LiDAR scanning strategy aimed to characterize atmospheric turbulent flows implies finding a trade-off between a sufficiently fine data spacing, which is quantified through Δd in the present work (Eq.(7)), and an adequate number of
325 time realizations, L, to reduce the temporal statistical uncertainty. Considering a total sampling period T, for which statistical stationarity can be assumed, and a pulsed LiDAR that scans N_r points evenly spaced along the LiDAR laser beam, with a range gate Δr and accumulation time τ_a, the total number of collected velocity samples is then equal to $N_s = N_r \cdot T/\tau_a$. The angular resolution of the LiDAR scanning head, $\Delta\theta$, can be selected to modify the angular spacing between consecutive line-of-sights (i.e. the data spacing) and the total sampling period for a single scan, τ_s (i.e. the number of realizations, L).

Table 2. Selected combinations of σ and m to achieve a $\sim$95% recovery of the mean of the selected fundamental half-wavelength and associated response of the higher-order moments (HOM).

	N = 2				N = 3		
σ	m	D^m (mean)	D^0 HOM	σ	m	D^m (mean)	D^0 (HOM)
1/3	6	0.942	0.334	1/4	5	0.952	0.397
1/4	3	0.955	0.540	1/6	2	0.961	0.663
1/6	1	0.942	0.76	1/8	1	0.957	0.793
1/13	0	0.943	0.943	1/17	0	0.950	0.950

The design of a LiDAR scan aiming to reconstruct turbulent statistics of an ergodic flow thorough LiSBOA can be formalized as a two-objective (or Pareto front) optimization problem. The first cost function of the Pareto front, which is referred to as ϵ^I, is the percentage of grid nodes for which the Petersen-Middleton constraint applied to the smallest half-wavelength of interest (i.e. $\boldsymbol{\Delta n_0}$), is not satisfied. In respect to the scaled reference frame, this can be expressed as:

$$\epsilon^I(\Delta\theta,\sigma) = \frac{\sum_{i=1}^{N_i}[\Delta\tilde{d} > 1]}{N_i},\tag{13}$$

where the square brackets are Iverson brackets and N_i is the total number of nodes in the Cartesian grid, $\boldsymbol{r_i}$. For a more conservative formulation, it is recommended to reject all the points with a distance smaller than $R_{\max}$ from an under-sampled grid node, i.e. with $\Delta\tilde{d} > 1$. This condition will ensure that the statistics are based solely on regions that are adequately sampled. The cost function ϵ^I depends not only on the angular resolution but also on $R_{\max}$, which is equal to 3σ in this work. In general, increasing σ results in a larger number of samples considered for the calculation of the statistics at each grid point $\boldsymbol{r_i}$ and, thus, in a reduction of ϵ^I. Therefore, a larger σ entails a larger percentage of the spatial domain fulfilling the Petersen-Middleton constraint. The smoothing parameter, σ, also plays a fundamental role in the response of higher-order statistical moments. Specifically, if the reconstruction of the variance or higher-order statistics is important, the response $D^0(\boldsymbol{\Delta\tilde{n}_0})$ should be included in the Pareto front analysis as an additional constraint.

The second cost function for the optimal design of LiDAR scans, ϵ^{II}, is equal to the standard deviation of the sample mean, which, for an autocorrelated signal, is (Bayley and Hammersley, 1946):

$$\epsilon^{II}(\Delta\theta) = \sqrt{\overline{u'^2}}\sqrt{\frac{1}{L} + \frac{2}{L^2}\sum_{p=1}^{L-1}(L-p)\,\rho_p} \sim \sqrt{\overline{u'^2}}\sqrt{\frac{1}{L} + \frac{2}{L^2}\sum_{p=1}^{L-1}(L-p)\,e^{-\frac{\tau_s}{\tau}p}},\tag{14}$$

where ρ_p is the autocorrelation function at lag p, τ is the integral time-scale and the approximation is based on George et al. (1978). The velocity variance, $\sqrt{\overline{u'^2}}$, and the autocorrelation, ρ_p, are functions of space; however, to a good degree of approximation, they can be replaced by a representative value and considered as uniform in space. Figure 6 shows the standard deviation of the sample mean normalized by the standard deviation of the velocity as a function of the number of realizations, L, and for different integral time-scales, τ. It is noteworthy that the standard deviation of the sample mean represents the uncertainty of the time-average of each measurement point, $\boldsymbol{r_j}$, while the final uncertainty of the mean field at the grid nodes $\boldsymbol{r_i}$ is generally reduced due to the spatial averaging process intrinsic to the LiSBOA.

The whole procedure for the design of a LiDAR scan and retrieval of the statistics is reported in the flow chart of Fig. 7. Summarizing, from a preliminary analysis of the velocity field under investigation, we determine the maximum total sampling time, T, the characteristic integral time-scale, τ, the characteristic velocity variance, $\overline{u'^2}$, the fundamental half-wavelengths $\boldsymbol{\Delta n_0}$. This information, together with the settings of the LiDAR (namely, the accumulation time, τ_a, the number of points per beam, N_r, and the gate length, Δr), allow for generating the Pareto front as a function of $\Delta\theta$ and for different values of σ. Based on the specific goals of the LiDAR campaign in terms of coverage of the selected domain (i.e. ϵ^I), statistical significance of the data (i.e. ϵ^{II}) and, eventually, response of the higher-order statistical moments (i.e. $D^0(\boldsymbol{\Delta\tilde{n}_0})$), the LiSBOA user should select the optimal angular resolution, $\Delta\theta$, and the set of allowable σ values. Due to the above-mentioned non-ideal effects on the
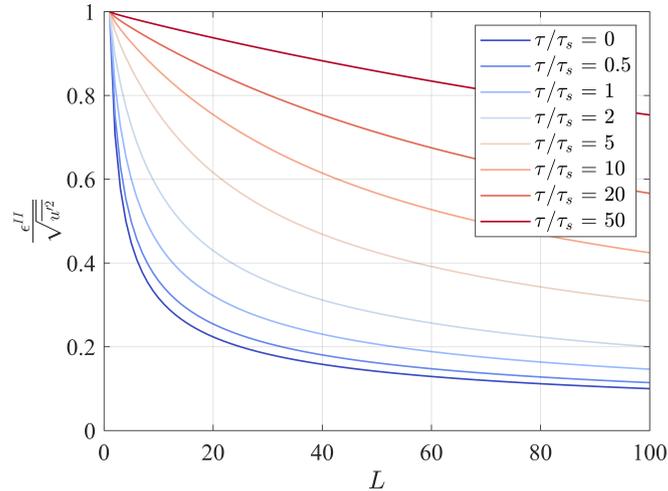
Figure 6. Standard deviation of the sample mean normalized by the standard deviation of velocity as a function of the number of realizations, L, and for different values of the ratio between the integral time-scale and the sampling time, τ/τ_s.
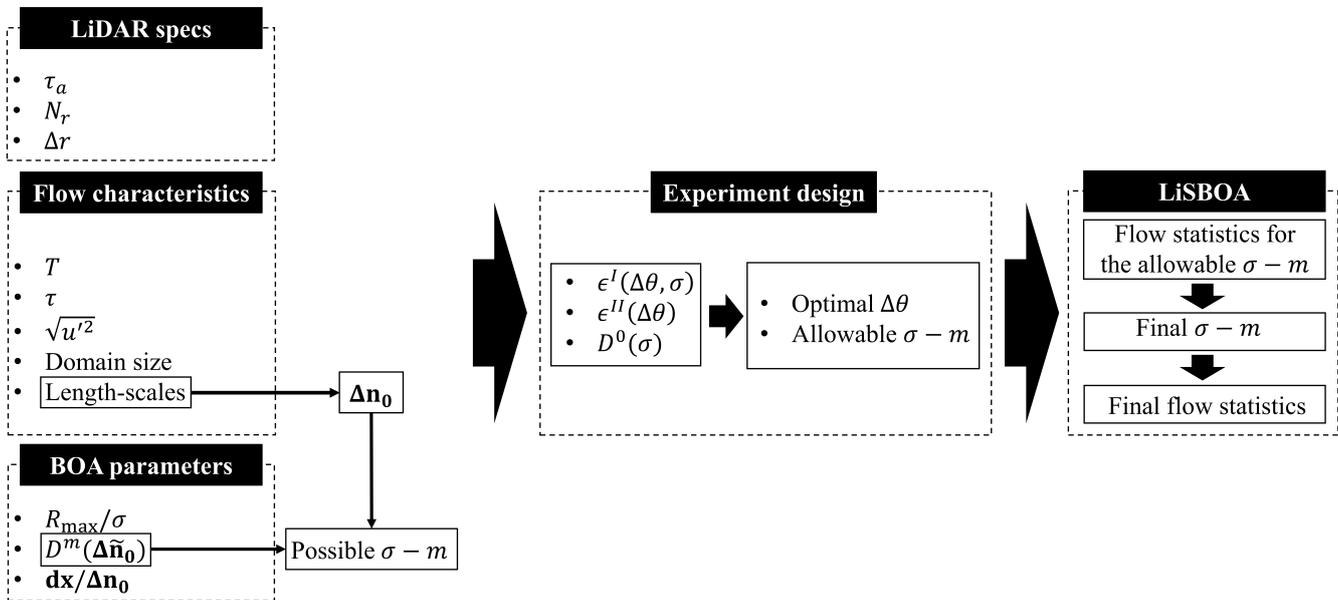
Figure 7. Schematic of the LiSBOA procedure for the optimal design of LiDAR scans and reconstruction of the statistics for a turbulent ergodic flow.

LiSBOA, the selection of σ is finalized during the post-processing phase when the LiDAR dataset is available and the statistics can be calculated for different pairs of $\sigma - m$ values. For the resolution of the Cartesian grid, Koch et al. (1983) suggested that it should be chosen as a fraction of the data spacing, which, in turn, is linked to the fundamental half-wavelength. The

same author suggested a grid spacing included in the range $dx \in [\Delta n_0/3, \Delta n_0/2]$. In this work, we have used $dx = \Delta n_0/4$, which ensures a good grid resolution with acceptable computational costs.

By following the steps outlined in the present section, the mean, variance, or even higher-order statistical moments of the velocity field can be accurately reconstructed for the wavelengths of interest. It is worth mentioning that the LiSBOA of wind LiDAR data should always be combined with a robust quality-control process of the raw measurements. Indeed, the space-time averaging operated by the LiSBOA makes the data analysis sensitive to the presence of data outliers, which need to be identified and rejected beforehand to prevent contamination of the final statistics.

5   Conclusions

A revisited Barnes objective analysis for sparse and non-uniformly distributed LiDAR data has been formulated to calculate mean, variance, and higher-order statistics of the wind velocity field over a structured N-dimensional Cartesian grid. This LiDAR Statistical Barnes Objective Analysis (LiSBOA) provides a theoretical framework to quantify the response in the reconstruction of the velocity statistics as a function of the spatial wavelengths of the velocity field under investigation and quantification of the sampling error. The LiSBOA has been validated against volumetric synthetic 3D data generated through Monte-Carlo simulations. The results of this test have shown that the sampling error for a monochromatic scalar field is mainly driven by the data spacing normalized by the half-wavelength.

Guidelines for the optimal design of scans performed with a scanning Doppler pulsed wind LiDAR and calculation of wind velocity statistics have been provided by leveraging the LiSBOA. The optimization problem consists in providing background information about the turbulent flow under investigation, such as expected velocity variance and integral length scales, technical specifications of the LiDAR, such as range gate and accumulation time, and spatial wavelengths of interest for the velocity field. The formulated optimization problem has two cost functions, namely the percentage of grid nodes not satisfying the Petersen-Middleton constraint for the smallest half-wavelength of interest (i.e. lacking adequate spatial resolution to avoid aliasing in the statistics), and the standard deviation of the sample mean. The output of the optimization problem are the LiDAR angular resolution and, for a given response of the mean field, the allowable smoothing parameters and number of iterations to use for the LiSBOA.

In the companion paper (Letizia et al.), the LiSBOA is applied to velocity fields associated with wind turbine wakes obtained through large-eddy simulations and LiDAR measurements. As a final note, this work is intended to contribute to the improvement and standardization of the LiDAR data collection and analysis methodology. We believe that the formulation of validated tools for quantitative analysis of LiDAR data represents an important process to unleash the full potential of the scanning LiDAR technology for investigations of atmospheric turbulent flows.

Code availability. The LiSBOA algorithm is implemented in a publicly available code which can be downloaded at the following URL: https://www.utdallas.edu/windflux/.

Appendix A: Derivation of the analytical response function of the LiSBOA

The first iteration of the LiSBOA produces a weighted average in space of the scalar field, f, with the weights being Gaussian functions centered at the specific grid nodes, $\boldsymbol{x}$. In the limit of a continuous function defined over an infinite domain, Eq. (3) represents the convolution between the scalar field, f, and the Gaussian weights, w. Therefore, the response function of the LiSBOA, can be expressed in the spectral domain as (Pauley and Wu, 1990):

$$D^0 = \frac{\mathfrak{F}[g^0]}{\mathfrak{F}[f]} = \mathfrak{F}[w], \tag{A1}$$

where the operator $\mathfrak{F}$ indicates the Fourier transform (FT). The FT of the weighting function in Eq. (A1) can be conveniently recast as the product of N one-dimensional FT:

$$\mathfrak{F}[w] = \prod_{p=1}^{N} \int_{-\infty}^{\infty} \frac{1}{\sqrt{2\pi}\sigma} e^{\frac{-x_p^2}{2\sigma^2}} \cdot e^{-\mathrm{i}k_p x_p} dx_p, \tag{A2}$$

where k_p is the directional wavenumber and $\mathrm{i} = \sqrt{-1}$. Hence, by leveraging the closed-form FT of the Gaussian function (Greenberg, 1998):

$$\mathfrak{F}\left[\frac{1}{\sqrt{2\pi}\sigma} e^{\frac{-x^2}{2\sigma^2}}\right] = e^{\frac{-k^2\sigma^2}{2}} \tag{A3}$$

we get the desired results, i.e.:

$$D^0(\boldsymbol{k}) = e^{-\frac{\sigma^2}{2}|\mathbf{k}|^2}. \tag{A4}$$

Author contributions. SL and GVI developed the LiSBOA and prepared the manuscript. The LiDAR data were generated as a team effort including contributions from all three authors. SL implemented the LiSBOA in a Matlab code under the supervision of GVI.

Competing interests. No competing interests are present.

Acknowledgements. This research has been funded by a grant from the National Science Foundation CBET Fluid Dynamics, award number 1705837. This material is based upon work supported by the National Science Foundation under grant IIP-1362022 (Collaborative Research: I/UCRC for Wind Energy, Science, Technology, and Research) and from the WindSTAR I/UCRC Members: Aquanis, Inc., EDP Renewables, Bachmann Electronic Corp., GE Energy, Huntsman, Hexion, Leeward Asset Management, LLC, Pattern Energy, EPRI, LM Wind, Texas Wind Tower and TPI Composites. Any opinions, findings, and conclusions or recommendations expressed in this material are those of the authors and do not necessarily reflect the views of the sponsors. Texas Advanced Computing Center is acknowledged for providing computational resources.

References

Achtemeier, G. L.: The Impact of Data Boundaries upon a Successive Corrections Objective Analysis of Limited-Area Datasets, Mon. Weather Rev., 114, 40–49, https://doi.org/10.1175/1520-0493(1986)114<0040:TIODBU>2.0.CO;2, 1986.

Achtemeier, G. L.: Modification of a Successive Corrections Objective Analysis for Improved Derivative Calculations, Mon. Weather Rev., 117, 78–86, https://doi.org/10.1175/1520-0493(1989)117<0078:MOASCO>2.0.CO;2, 1989.

Aitken, M. L. and Lundquist, J. K.: Utility-Scale Wind Turbine Wake Characterization Using Nacelle-Based Long-Range Scanning Lidar, J. Atmos. Ocean. Tech., 31, 1529–1539, https://doi.org/10.1175/JTECH-D-13-00218.1, 2014.

Arenas, I., García, E., Fu, M. K., Orlandi, P., Hultmark, M., and Leonardi, S.: Comparison between super-hydrophobic, liquid infused and rough surfaces: a direct numerical simulation study, J. Fluid Mech., 869, 500–525, https://doi.org/10.1017/jfm.2019.222, 2019.

Askelson, M. A., Aubagnac, J. P., and Straka, J. M.: An Adaptation of the Barnes Filter Applied to the Objective Analysis of Radar Data, Mon. Weather Rev., 128, 3050–3082, https://doi.org/10.1175/1520-0493(2000)128<3050:AAOTBF>2.0.CO;2, 2000.

Astrup, P., Mikkelsen, T. K., and van Dooren, M. F.: Wind field determination from multiple Spinner-Lidar line-of-sight measurements using linearized CFD, DTU Wind Energy E. 0102, DTU, Department of Wind Energy Frederiksborgvej 399 DK-4000 Roskilde Denmark, 2017.

Banakh, V. A., Smalikho, I. N., Köpp, F., and Werner, C.: Measurements of Turbulent Energy Dissipation Rate with a CW Doppler Lidar in the Atmospheric Boundary Layer, J. Atmos. Ocean. Tech., 16, 1044–1061, https://doi.org/10.1175/1520-0426(1999)016<1044:MOTEDR>2.0.CO;2, 1999.

Banta, R. M., Pichugina, Y. L., and Brewer, W. A.: Turbulent Velocity-Variance Profiles in the Stable Boundary Layer Generated by a Nocturnal Low-Level Jet, J. Atmos. Sci., 63, 2700–2719, https://doi.org/10.1175/JAS3776.1, 2006.

Barnes, S.: Application of Barnes Objective Analysis scheme. Part III: tuning for minimum error., J. Atmos. Ocean. Tech., 11, 1449–1458, https://doi.org/10.1175/1520-0426(1994)011<1459:AOTBOA>2.0.CO;2, 1994c.

Barnes, S. L.: A Technique for Maximizing Details in Numerical Weather Map Analysis, J. Appl. Meteorol., 3, 396–409, https://doi.org/10.1175/1520-0450(1964)003<0396:ATFMDI>2.0.CO;2, 1964.

Barnes, S. L.: Mesoscale Objective Map Analysis Using Weighted Time-Series Observations, NOAA Technical Memorandum ERL NSSL-62, National Severe Storms Laboratory Norman, National Severe Storms Laboratory Norman, OK, 1973.

Barnes, S. L.: Applications of the Barnes Objective Analysis Scheme. Part I: Effects of Undersampling, Wave Position, and Station Randomness, J. Atmos. Ocean. Tech., 11, 1433–1448, https://doi.org/10.1175/1520-0426(1994)011<1433:AOTBOA>2.0.CO;2, 1994a.

Bayley, V. G. and Hammersley, J. M.: The "Effective" Number of Independent Observations in an Autocorrelated Time Series, Supplement to the Journal of Royal Statistical Society, 8, 184–197, 1946.

Beck, H. and Kühn, M.: Dynamic Data Filtering of Long-Range Doppler LiDAR Wind Speed Measurements, Remote Sens.-Basel, 9, 561, 2017.

Bell, T. M., Klein, P., Wildmann, N., and Menke, R.: Analysis of flow in complex terrain using multi-Doppler lidar retrievals, Atmos. Meas. Tech., 13, 1357–1371, https://doi.org/10.5194/amt-13-1357-2020, 2020.

Berg, J., Mann, J., Bechmann, A., Courtney, M. S., and Jørgensen, H. E.: The Bolund Experiment. Part I : Flow Over a Steep, Three-dimensional Hill, Bound.-Lay. Meteorol., pp. 219–243, https://doi.org/10.1007/s10546-011-9636-y, 2011.

Bingöl, F.: Complex terrain and wind lidars, DTU PhD Thesis Risø-PhD-52, Technical Univeristy of Denmark, DTU Vindenergi Nils Koppels Allé Bygning 403 2800 Kgs. Lyngby, 2009.

Bingöl, F., Mann, J., and Larsen, G. C.: Light detection and ranging measurements of wake dynamics. Part I: one-dimensional scanning, Wind Energy, 13, 51–61, https://doi.org/10.1002/we.352, 2010.

Bodini, N., Zardi, D., and Lundquist, J. K.: Three-dimensional structure of wind turbine wakes as measured by scanning lidar, Atmos. Meas. Tech., 10, 2881–2896, https://doi.org/10.5194/amt-10-2881-2017, 2017.

460 Bonin, T. A., Choukulkar, A., Brewer, W. A., Sandberg, S. P., Weickmann, A. M., Pichugina, Y. L., Banta, R. A., Oncley, S. P., and Wolfe, D. E.: Evaluation of turbulence measurement techniques from a single Doppler lidar, Atmos. Meas. Tech., 10, 3021–3039, https://doi.org/10.5194/amt-10-3021-2017, https://www.atmos-meas-tech.net/10/3021/2017/, 2017.

Bradley, E. F.: The influence of thermal stability and angle of incidence on the acceleration of wind up a slope, J. Wind Eng. Ind. Aerod., 15, 231–242, 1983.

465 Braham, R. R.: Field Experimentation in Weather Modification, J. Am. Stat. Assoc., 74, 57–68, http://www.jstor.org/stable/2286722, 1979.

Bromm, M., Rott, A., Beck, H., Vollmer, L., Steinfeld, G., and Kühn, M.: Field investigation on the influence of yaw misalignment on the propagation of wind turbine wakes, Wind Energy, 21, 1011–1028, https://doi.org/10.1002/we.2210, 2018.

Buzzi, A., D Gomis, D., A., P. M., and Alonso, S.: A Method to Reduce the Adverse Impact that Inhomogeneous Station Distributions Have on Spatial Interpolation, Mon. Weather Rev., 119, 2465–2491, https://doi.org/10.1175/1520-0493(1991)119<2465:AMTRTA>2.0.CO;2, 470 1991.

Caracena, F.: Analytic Approximation of Discrete Field Samples with Weighted Sums and the Gridless Computation of Field Derivatives, J. Atmos. Sci., 44, 3753–3768, https://doi.org/10.1175/1520-0469(1987)044<3753:AAODFS>2.0.CO;2, 1987.

Caracena, F., Barnes, S. L., and Doswell III, C.: Weighting function parameters for objective interpolation of meteorological data, in: Preprints, 10-th Conf. on Weather Forecasting and Analysis, pp. 109–116, 1984.

475 Carbajo Fuertes, F., Markfort, C. D., and Porté-Agel, F.: Wind Turbine Wake Characterization with Nacelle-Mounted Wind Lidars for Analytical Wake Model Validation, Remote Sens.-Basel, 10, https://doi.org/10.3390/rs10050668, 2018.

Choukulkar, A., Brewer, W. A., Sandberg, S. P., Weickmann, A., Bonin, T. A., Hardesty, R. M., Lundquist, J. K., Delgado, R., Iungo, G. V., Ashton, R., Debnath, M., Bianco, L., Wilczak, J. M., Oncley, S., and Wolfe, D.: Evaluation of single and multiple Doppler lidar techniques to measure complex flow during the XPIA field campaign, Atmos. Meas. Tech., 10, 247–264, https://doi.org/10.5194/amt-10-247-2017, 480 2017.

Clive, P. J. M., Dinwoodie, I., and Quail, F.: Direct measurement of wind turbine wakes using Remote Sens.-Basel, Proceedings of the EWEA, 2011.

Cressman, G. P.: An Operational Objective Analysis System, Mon. Weather Rev., 87, 367–374, https://doi.org/10.1175/1520-0493(1959)087<0367:AOOAS>2.0.CO;2, 1959.

485 Cuerva, A. and Sanz-Andrés, A.: On sonic anemometer measurement theory, J. Wind Eng. Ind. Aerod., 88, 25–55, https://doi.org/10.1016/S0167-6105(00)00023-4, 2000.

Cushman-Roisin, B. and Beckers, J. M.: Introduction, in: Introduction to Geophysical Fluid Dynamics, pp. 7–11, Academic Press, 1990a.

Cushman-Roisin, B. and Beckers, J. M.: Stratification effects, in: Introduction to Geophysical Fluid Dynamics, p. 319, Academic Press, 1990b.

490 Davies, F., Middleton, D. R., and Bozier, K. E.: Urban air pollution modelling and measurements of boundary layer height, Atmos. Environ., 41, 4040–4049, https://doi.org/10.1016/j.atmosenv.2007.01.015, 2007.

Debnath, M., Iungo, G. V., Ashton, R., Alan Brewer, W., Choukulkar, A., Delgado, R., Lundquist, J. K., Shaw, W. J., Wilczak, J. M., and Wolfe, D.: Vertical profiles of the 3-D wind velocity retrieved from multiple wind lidars performing triple range-height-indicator scans, Atmos. Meas. Tech., 10, 431–444, https://doi.org/10.5194/amt-10-431-2017, 2017a.

495 Debnath, M., Iungo, G. V., Brewer, W. A., Choukulkar, A., Delgado, R., Gunter, S., Lundquist, J. K., Schroeder, J. L., Wilczak, J. M., and Wolfe, D.: Assessment of virtual towers performed with scanning wind lidars and Ka-band radars during the XPIA experiment, Atmos. Meas. Tech., pp. 1215–1227, https://doi.org/10.5194/amt-10-1215-2017, 2017b.

Doswell, C. A.: Obtaining Meteorologically Significant Surface Divergence Fields Through the Filtering Property of Objective Analysis, Mon. Weather Rev., 105, 885–892, https://doi.org/10.1175/1520-0493(1977)105<0885:OMSSDF>2.0.CO;2, 1977.

500 Duncan, Jr., J. B., Hirth, B. D., and Schroeder, J. L.: Enhanced estimation of boundary layer advective properties to improve space-to-time conversion processes for wind energy applications, Wind Energy, 22, 1203–1218, https://doi.org/10.1002/we.2350, https://onlinelibrary.wiley.com/doi/abs/10.1002/we.2350, 2019.

Eberhard, W. L., Cupp, R. E., and Healy, K. R.: Doppler Lidar Measurement of Profiles of Turbulence and Momentum Flux, J. Atmos. Ocean. Tech., 6, 809–819, https://doi.org/10.1175/1520-0426(1989)006<0809:DLMOPO>2.0.CO;2, 1989.

505 El-Asha, S., Zhan, L., and Iungo, G. V.: Quantification of power losses due to wind turbine wake interactions through SCADA, meteorological and wind LiDAR data, Wind Energy, 20, 1823–1839, https://doi.org/10.1002/we.2123, 2017.

Emeis, S.: Surface-Based Remote Sensing of the Atmospheric Boundary Layer, Springer: Berlin/Heidelberg, 2010.

Emeis, S., Frank, H. R., and Fiedler, F.: Modification of air flow over an escarpment - Results from the Hjardemal experiment, Bound.-Lay. Meteorol., 74, 131–161, 1995.

510 Endlich, R. M. and Mancuso, R. L.: Objective analysis of environmental conditions associated with severe thunderstorms and tornadoes, Mon. Weather Rev., 96, 342–350, https://doi.org/10.1126/science.27.693.594, 1968.

Fernando, H. J. S., Mann, J., Palma, J. M. L. M., Lundquist, J. K., Barthelmie, R. J., Belo-Pereira, M., Brown, W., Chow, F. K., and Gerz, T., e. a.: Peering into microscale details of mountain winds, B. Am. Meteorol. Soc., 100, 799–820, https://doi.org/10.1175/BAMS-D-17-0227.1, 2019.

515 Frehlich, R. and Cornman, L.: Estimating Spatial Velocity Statistics with Coherent Doppler Lidar, J. Atmos. Ocean. Tech., 19, 355–366, https://doi.org/10.1175/1520-0426-19.3.355, 2002.

Frisch, A. S.: On the measurement of second moments of turbulent wind velocity with a single Doppler radar over non-homogeneous terrain, Bound.-Lay. Meteorol., 54, 29–39, 1991.

Fuertes Carbajo, F. and Porté-Agel, F.: Using a Virtual Lidar Approach to Assess the Accuracy of the Volumetric Reconstruction of a Wind
520 Turbine Wake, Remote Sens.-Basel, 10, https://doi.org/10.3390/rs10050721, 2018.

Gal-Chen, T., Xu, M., and Eberhard, W. L.: Estimations of atmospheric boundary layer fluxes and other turbulence parameters from Doppler lidar data, J. Geophys. Res.-Atmos., 97, 18 409–18 423, https://doi.org/10.1029/91JD03174, 1992.

Garcia, E. T., Aubrun, S., a. B. M., Royer, P., Coupiac, O., and Girard, N.: Wake meandering and its relationship with the incoming wind characteristics: a statistical approach applied to long-term on-field observations, Journal of Physics: Conference Series, 854, 012 045,
525 https://doi.org/10.1088/1742-6596/854/1/012045, 2017.

George, W., Beuther, P. D., and Lumley, J. L.: Processing of Random Signals, in: Proceedings of the Dynamic Flow Conference, pp. 757–800, 1978.

Gomis, D. and Alonso, S.: Diagnosis of a Cyclogenetic Event in the Western Mediterranean Using an Objective Technique for Scale Separation, Mon. Weather Rev., 118, 723–736, https://doi.org/10.1175/1520-0493(1990)118<0723:DOACEI>2.0.CO;2, 1990.

530   Greenberg, M.: Advanced Engineering Mathematics, 2nd edition, Prentice Hall, 1998.

Halios, C. H. and Barlow, J. F.: Observations of the Morning Development of the Urban Boundary Layer Over London, UK, Taken During the ACTUAL Project, Bound.-Lay. Meteorol., 166, 395–422, https://doi.org/10.1007/s10546-017-0300-z, 2018.

Haugen, D. A., Kaimal, J. C., and Bradley, E. F.: An experimental study of Reynolds stress and heat flux in the atmospheric surface layer, Q. J. Roy. Meteorol. Soc., 97, 168–180, https://doi.org/10.1002/qj.49709741204, 1971.

535   Holzäpfel, F., Stephan, A., Heel, T., and Körner, S.: Enhanced wake vortex decay in ground proximity triggered by plate lines, Aircr. Eng.g Aerosp.Tech., 88, 206–214, https://doi.org/10.1108/AEAT-02-2015-0045, 2016.

Huang, M., Gao, Z., Miao, S., Chen, F., LeMone, M. A., Li, J., Hu, F., and Wang, L.: Estimate of Boundary-Layer Depth Over Beijing, China, Using Doppler Lidar Data During SURF-2015, Bound.-Lay. Meteorol., 162, 503–522, https://doi.org/10.1007/s10546-016-0205-2, 2017.

Iungo, G. V. and Porté-Agel, F.: Volumetric Lidar Scanning of Wind Turbine Wakes under Convective and Neutral Atmospheric Stability
540   Regimes, J. Atmos. Ocean. Tech., 31, 2035–2048, https://doi.org/10.1175/JTECH-D-13-00252.1, 2014.

Iungo, G. V., Wu, Y., and Porté-Agel, F.: Field Measurements of Wind Turbine Wakes with Lidars, J. Atmos. Ocean. Tech., 30, 274–287, https://doi.org/10.1175/JTECH-D-12-00051.1, 2013.

Käsler, Y., S., R., Simmet, R., and Kühn, M.: Wake Measurements of a Multi-MW Wind Turbine with Coherent Long-Range Pulsed Doppler Wind Lidar, J. Atmos. Ocean. Tech., 27, 1529–1532, https://doi.org/10.1175/2010JTECHA1483.1, 2010.

545   Kim, D., Kim, T., Oh, G., Huh, J., and Ko, K.: A comparison of ground-based LiDAR and met mast wind measurements for wind resource assessment over various terrain conditions, J. Wind Eng. Ind. Aerod., 158, 109–121, https://doi.org/10.1016/j.jweia.2016.09.011, http://dx.doi.org/10.1016/j.jweia.2016.09.011, 2016.

Koch, S. E., Des Jardins, M., and Kocin, P. J.: An Interactive Barnes objective Map Analysis Scheme for Use with Satellite and Conventional Data, J. Clim. Appl. Meteorol., 22, 1487–1503, https://doi.org/10.1175/1520-0450(1983)022<1487:AIBOMA>2.0.CO;2, 1983.

550   Kongara, S., Calhoun, R., Choukulkar, A., and Boldi, M. O.: Velocity retrieval for coherent Doppler lidar, Int. J. Remote Sens., 33, 3596–3613, https://doi.org/10.1080/01431161.2011.631948, 2012.

Köpp, F., Rahm, S., Smalikho, I., Dolfi, A., Cariou, J. P., Harris, M., and Young, R. I.: Comparison of wake-vortex parameters measured by pulsed and continuous-wave lidars, J. Aircraft, 42, 916–923, https://doi.org/10.2514/1.8177, 2005.

Krishnamurthy, R., Choukulkar, A., Calhoun, R., Fine, J., Oliver, A., and Barr, K. S.: Coherent Doppler lidar for wind farm characterization,
555   Wind Energy, 16, 189–206, https://doi.org/10.1002/we, 2013.

Kropfli, R. A.: Single Doppler Radar Measurements of Turbulence Profiles in the Convective Boundary Layer, J. Atmos. Ocean. Tech., 3, 305–314, https://doi.org/10.1175/1520-0426(1986)003<0305:SDRMOT>2.0.CO;2, 1986.

Kumer, V. M., Reudera, J., Svardalc, B., Sætrec, C., and Eecen, P.: Characterisation of Single Wind Turbine Wakes with Static and Scanning WINTWEX-W LiDAR Data, Energy Proced., 80, 245 – 254, https://doi.org/https://doi.org/10.1016/j.egypro.2015.11.428, 12th Deep Sea
560   Offshore Wind R and D Conference, EERA DeepWind 2015, 2015.

Kunkel, G. J. and Marusic, I.: Study of the near-wall-turbulent region of the high-Reynolds-number boundary layer using an atmospheric flow, J. Fluid Mech., 548, 375–402, https://doi.org/10.1017/S0022112005007780, 2006.

Letizia, S., Zhan, L., and Iungo, G. V.: LiSBOA: LiDAR Statistical Barnes Objective Analysis for optimal design of1LiDAR scans and retrieval of wind statistics. Part II: Applications to synthetic and real LiDAR data of wind turbine wakes .

565   Lhermitte, R. M.: Note on the Observation of Small-Scale Atmospheric Turbulence by Doppler Radar Techniques, Radio Sci., 4, 1241–1246, https://doi.org/10.1029/RS004i012p01241, 1969.

Liu, Z., Barlow, J. F., Chan, P. W., Fung, J. C. H., Li, Y., Ren, C., Mak, H. W. L., and Ng, E.: A review of progress and applications of pulsed Doppler Wind LiDARs, Remote Sens.-Basel, 11, 1–47, https://doi.org/10.3390/rs11212522, 2019.

Lundquist, J. K., Wilczak, J. M., Ashton, R., Bianco, L., Brewer, W. A., Choukulkar, A., Clifton, A., Debnath, M., Delgado, R., Friedrich, K., Gunter, S., Hamidi, A., Iungo, G. V., Kaushik, A., Kosovic, B., Langan, P., Lass, A., Lavin, E., Lee, J. C. Y., McCaffrey, K. L., Newsom, R. K., Noone, D. C., Oncley, S. P., ., Quelet, P. T., Sandberg, S. P., Schroeder, J. L., Shaw, W. J., Sparling, L., Martin, C. S., Pe, A. S., Strobach, E., Tay, K., Vanderwende, B. J., Weickmann, A., Wolfe, D., and Worsnop, R.: Assessing state-of-The-Art capabilities for probing the atmospheric boundary layer the XPIA field campaign, B. Am. Meteorol. Soc., 98, 289–314, https://doi.org/10.1175/BAMS-D-15-00151.1, 2017.

Machefaux, E., Larsen, G. C., Troldborg, N., Hansen, K. S., Angelou, N., Mikkelsen, T., and Mann, J.: Investigation of wake interaction using full-scale lidar measurements and large eddy simulation, Wind Energy, 19, 1535–1551, https://doi.org/10.1002/we.1936, 2016.

Maddox, R. A.: An Objective Technique for Separating Macroscale and Mesoscale Features in Meteorological Data, Mon. Weather Rev., 108, 1108–1121, https://doi.org/10.1175/1520-0493(1980)108<1108:AOTFSM>2.0.CO;2, 1980.

Mann, J., Peña, A., Bingöl, F., Wagner, R., and Courtney, M. S.: Lidar Scanning of Momentum Flux in and above the Atmospheric Surface Layer, J. Atmos. Ocean. Tech., 27, 959–976, https://doi.org/10.1175/2010JTECHA1389.1, 2010.

Mayor, S. D., Lenschow, D. H., Schwiesow, R. L., Mann, J., Frush, C. L., and Simon, M. K.: Validation of NCAR 10.6-μm CO2 Doppler Lidar Radial Velocity Measurements and Comparison with a 915-MHz Profiler, J. Atmos. Ocean. Tech., 14, 1110–1126, https://doi.org/10.1175/1520-0426(1997)014<1110:VONMCD>2.0.CO;2, 1997.

Mortensen, N. G.: Wind measurements for wind energy applications—a review, Proceedings of the 16th British Wind Energy Association Conference', Stirling, Scotland, pp. 353–360, 1994.

Muñoz-Esparza, D., Cañadillas, B., Neumann, T., and Van Beeck, J.: Turbulent fluxes, stability and shear in the offshore environment: Mesoscale modelling and field observations at FINO1, J. Renew. Sustain. Ener., 4, https://doi.org/10.1063/1.4769201, 2012.

Newsom, R., Berg, L., Shaw, W. J., and Fischer, M. L.: Turbine-scale wind field measurements using dual-Doppler lidar, Wind Energy, 18, 219–235, https://doi.org/10.1002/we.1691, 2014.

Newsom, R. K. and Banta, R. M.: Assimilating Coherent Doppler Lidar Measurements into a Model of the Atmospheric Boundary Layer. Part I: Algorithm Development and Sensitivity to Measurement Error, J. Atmos. Ocean. Tech., 21, 1328–1345, https://doi.org/10.1175/1520-0426(2004)021<1328:ACDLMI>2.0.CO;2, 2004.

Newsom, R. K., Calhoun, R., Ligon, D., and Allwine, J.: Linearly Organized Turbulence Structures Observed Over a Suburban Area by Dual-Doppler Lidar, Bound.-Lay. Meteorol., 127, 111–130, https://doi.org/10.1007/s10546-007-9243-0, 2008.

Newsom, R. K., Alan Brewer, W., Wilczak, J. M., Wolfe, D. E., Oncley, S. P., and Lundquist, J. K.: Validating precision estimates in horizontal wind measurements from a Doppler lidar, Atmos. Meas. Tech., 10, 1229–1240, https://doi.org/10.5194/amt-10-1229-2017, 2017.

O'Connor, E. J., Illingworth, A. J., Brooks, I. M., Westbrook, C. D., Hogan, R. J., Davies, F., and Brooks, B. J.: A Method for Estimating the Turbulent Kinetic Energy Dissipation Rate from a Vertically Pointing Doppler Lidar, and Independent Evaluation from Balloon-Borne In Situ Measurements, J. Atmos. Ocean. Tech., 27, 1652–1664, https://doi.org/10.1175/2010JTECHA1455.1, 2010.

Pardyjak, E. R. and Stoll, R.: Improving measurement technology for the design of sustainable cities, Meas. Sci. Technol., 28, https://doi.org/10.1088/1361-6501/aa7c77, 2017.

Pashow, M., Parlange, M. B., and Porté-Agel, F.: On Monin–Obukhov similarity in the stable atmospheric boundary layer, Bound.-Lay. Meteorol., 99, 225–248, https://doi.org/10.1023/A, 2001.

Pauley, P. M. and Wu, X.: The Theoretical, Discrete, and Actual Response of the Barnes Objective Analysis Scheme for One- and Two-Dimensional Fields, Mon. Weather Rev., 118, 1145–1164, https://doi.org/10.1175/1520-0493(1990)118<1145:TTDAAR>2.0.CO;2, 1990.

Pauscher, L., Vasiljevic, N., Callies, D., Lea, G., Mann, J., Klaas, T., Hieronimus, J., Gottschall, J., Schwesig, A., Kühn, M., and Courtney, M.: An inter-comparison study of multi- and DBS lidar measurements in complex terrain, Remote Sens.-Basel, 8, https://doi.org/10.3390/rs8090782, 2016.

Petersen, D. P. and Middleton, D.: Sampling and reconstruction of wave-number-limited functions in N-dimensional Euclidean spaces, Inform. Control., 5, 279–323, https://doi.org/10.1016/S0019-9958(62)90633-2, 1962.

Rajewski, D. A., Takle, E. S., Lundquist, J. K., Oncley, S., Prueger, J. H., Horst, T. W., Rhodes, M. E., Pfeiffer, R., Hatfield, J. L., Spoth, K. K., and Doorenbos, R. K.: Crop wind energy experiment (CWEX): Observations of surface-layer, boundary layer, and mesoscale interactions with a wind farm, B. Am. Meteorol. Soc., 94, 655–672, https://doi.org/10.1175/BAMS-D-11-00240.1, 2013.

Risan, A., Lund, J. A., Chang, C. Y., and Sætran, L.: Wind in Complex Terrain - Lidar Measurements for Evaluation of CFD Simulations, Remote Sens.-Basel, 10, 59, 2018.

Sasaki, Y.: A theoretical interpretation of anisotropically weighted smoothing on the basis of numerical variational analysis, Mon. Weather Rev., 99, 698–707, 1971.

Sathe, A. and Mann, J.: A review of turbulence measurements using ground-based wind lidars, Atmos. Meas. Tech., 6, 3147–3167, https://doi.org/10.5194/amt-6-3147-2013, https://www.atmos-meas-tech.net/6/3147/2013/, 2013.

Schween, J. H., Hirsikko, A., Löhnert, U., and Crewell, S.: Mixing-layer height retrieval with ceilometer and Doppler lidar: From case studies to long-term assessment, Atmos. Meas. Tech., 7, 3685–3704, https://doi.org/10.5194/amt-7-3685-2014, 2014.

Seaman, R. S.: Tuning the Barnes Objective Analysis Parameters by Statistical Interpolation Theory, J. Atmos. Ocean. Tech., 6, 993–1000, https://doi.org/10.1175/1520-0426(1989)006<0993:TTBOAP>2.0.CO;2, 1989.

Sekar, A. P. K., van Dooren, M. F., Mikkelsen, T., Sjöholm, M., Astrup, P., and Kühn, M.: Evaluation of the LINCOM wind field reconstruction method with simulations and full-scale measurements, Journal of Physics: Conference Series, 1037, 052 008, https://doi.org/10.1088/1742-6596/1037/5/052008, 2018.

Shannon, C. E.: Communication in the Presence of Noise, Proceedings of the IEEE, 72, 1192–1201, https://doi.org/10.1109/PROC.1984.12998, 1984.

Smalikho, I. N.: On measurement of dissipation rate of the turbulent energy with a CW lidar, Atmos. Ocean. Optics, 8, 788–793, 1995.

Smith, D. R. and Leslie, F. W.: Error Determination of a Successive Correction Type Objective Analysis Scheme, J. Atmos. Ocean. Tech., 1, 120–130, https://doi.org/10.1175/1520-0426(1984)001<0120:EDOASC>2.0.CO;2, 1984.

Smith, D. R., Pumphry, M. E., and Snow, J. T.: A Comparison of Errors in objectively Analyzed Fields for Uniform and Nonuniform Station Distributions, J. Atmos. Ocean. Tech., 3, 84–97, https://doi.org/10.1175/1520-0426(1986)003<0084:ACOEIO>2.0.CO;2, 1986.

Stull, R. B.: Preface, in: An introduction to Boundary Layer Meteorology, p. xi, Kluwer Academic Publisher, P.O. 80x 17. 3300 AA Dordredt. The NetherlandS, 1988.

Tang, W., Chan, P. W., and Haller, G.: Lagrangian coherent structure analysis of terminal winds detected by lidar. Part I: Turbulence structures, J. Appl. Meteorol. Clim., 50, 325–338, https://doi.org/10.1175/2010JAMC2508.1, 2011.

Taylor, P. A. and Teunissen, H. W.: The Askervin hill project: overview and background data, Bound.-Lay. Meteorol., 39, 15–39, 1987.

Thobois, L., Cariou, J. P., and Gultepe, I.: Review of Lidar-Based Applications for Aviation Weather, Pure Appl. Geophys., 176, 1959–1976, https://doi.org/10.1007/s00024-018-2058-8, 2019.

Trapp, R. J. and Doswell, C. A.: Radar data objective analysis, J. Atmos. Ocean. Tech., 17, 105–120, https://doi.org/10.1175/1520-0426(2000)017<0105:RDOA>2.0.CO;2, 2000.

Trujillo, J. J., F., B., Larsen, G. C., Mann, J., and Kühn, M.: Light detection and ranging measurements of wake dynamics. Part II: two-dimensional scanning, Wind Energy, 14, 61–75, https://doi.org/10.1002/we.402, 2011.

645 Trujillo, J. J., Seifert, J. K., Würth, I., Schlipf, D., and Kühn, M.: Full-field assessment of wind turbine near-wake deviation in relation to yaw misalignment, Wind Energy Science, 1, 41–53, https://doi.org/10.5194/wes-1-41-2016, 2016.

Vakkari, V., O'Connor, E. J., Nisantzi, A., Mamouri, R. E., and Hadjimitsis, D. G.: Low-level mixing height detection in coastal locations with a scanning Doppler lidar, Atmos. Meas. Tech., 8, 1875–1885, https://doi.org/10.5194/amt-8-1875-2015, 2015.

Van Dooren, M. F., Trabucchi, D., and Kühn, M.: A Methodology for the Reconstruction of 2D Horizontal Wind Fields of Wind Turbine
650 Wakes Based on Dual-Doppler Lidar Measurements, Remote Sens.-Basel, 8, https://doi.org/10.3390/rs8100809, 2016.

Wang, H. and Barthelmie, R. J.: Wind turbine wake detection with a single Doppler wind lidar, Journal of Physics: Conference Series, 625, 012 017, https://doi.org/10.1088/1742-6596/625/1/012017, 2015.

Wheeler, A. J., A. R. J.: Measuring Fluid Flow Rate, Fluid Velocity, Fluid Level and Combustion Pollutants, in: Introduction to engineering experimentation, pp. 366–368, Pearson Higher Education, 1 Lake St., Upper Saddle River, New Jersey, 07458., 2004.

655 Wilson, D. A.: Doppler Radar Studies of Boundary Layer, Wind Profiles and Turbulence in Snow Conditions, Proc. 14th Conference on Radar Meteorology, Tucson, USA, p. 191–196, 1970.

Xia, Q., Lin, C. L., Calhoun, R., and Newsom, R. K.: Retrieval of Urban Boundary Layer Structures from Doppler Lidar Data. Part I: Accuracy Assessment, J. Atmos. Sci., 65, 3–20, https://doi.org/10.1175/2007JAS2328.1, 2008.

Xu, Q. and Gong, J.: Background error covariance functions for Doppler radial-wind analysis, Q. J. Roy. Meteorol. Soc., 129, 1703–1720,
660 https://doi.org/10.1256/qj.02.129, 2002.

Zhan, L., Letizia, S., and Iungo, G. V.: LiDAR measurements for an onshore wind farm: Wake variability for different incoming wind speeds and atmospheric stability regimes, Wind Energy, pp. 1–27, https://doi.org/10.1002/we.2430, 2019.

Zhan, L., Letizia, S., and Iungo, G. V.: Wind LiDAR Measurements of Wind Turbine Wakes Evolving over Flat and Complex Terrains: Ensemble Statistics of the Velocity Field, Journal of Physics: Conference Series, 1452, https://doi.org/10.1088/1742-6596/1452/1/012077,
665 2020.